AIAA JOURNAL
Vol. 51, No. 4, April 2013

Large-Eddy Simulation of an Oscillating Cylinder in a Steady Flow

A. Feymark*
Chalmers University of Technology, 412 96 Gothenburg, Sweden
N. Alin†
Swedish Defense Research Agency, 147 25 Stockholm, Sweden
R. E. Bensow‡
Chalmers University of Technology, 412 96 Gothenburg, Sweden
and
C. Fureby§
Swedish Defense Research Agency, 147 25 Stockholm, Sweden

DOI: 10.2514/1.J050653

In this work, large-eddy simulation is used to study the flow around a circular cylinder undergoing streamwise sinusoidal oscillations. This benchmark case is a first step toward studying engineering applications related to flow-induced vibrations. Both the flow physics, which correlate the flow development with the time varying loading of the cylinder at two different oscillation frequencies, as well as a validation of the fluid structure interaction methodology through comparison with experimental data for the same configuration are described. With the methodology used, large-eddy simulation based on a finite volume method capable of handling moving meshes gives force predictions that generally agree well with experimentally measured data, both with respect to the overall flow development as with force magnitude.

Nomenclature

α_i	=	coefficients of the time integration scheme
A	=	amplitude of cylinder oscillation
β_i	=	coefficients of the time integration scheme
C_p	=	pressure coefficient
C_x	=	force coefficient in the x direction
C_y	=	force coefficient in the y direction
D	=	cylinder diameter
$\mathbf{D}$	=	rate-of-strain tensor
$d\mathbf{A}_f$	=	area of cell face f of Ω_P
f	=	frequency
G	=	filter kernel
h_0	=	vertical distance from the free surface down to the center of the cylinder
k	=	subgrid kinetic energy
L	=	length of the cylinder
ℓ	=	distance to the wall
ℓ_I	=	integral length scale
ℓ_K	=	Kolmogorov microscale
ℓ_T	=	Taylor microscale
m	=	commutation error term
m	=	coefficient of the time integration scheme
$\mathbf{m}$	=	commutation error term
$\mathbf{n}$	=	normal direction
p	=	pressure
p_0	=	pressure at the outlet
Re	=	Reynolds number
$\mathbf{S}$	=	viscous stress tensor
St	=	Strouhal number
T	=	oscillation period
t	=	time
u_τ	=	friction velocity
$\mathbf{v}$	=	velocity
ν	=	viscosity
v'_k	=	subgrid velocity
$v'_{y,\mathrm{PW}}$	=	dimensionless velocity at the grid point closest to the wall
ν_{BC}	=	subgrid wall viscosity
v_c	=	velocity of the cylinder
ν_k	=	subgrid viscosity
$\mathbf{v}_m$	=	grid velocity
v_0	=	freestream velocity
$\hat{v}_c$	=	maximum velocity of the cylinder
x_c	=	displacement of the cylinder
$\mathbf{x}_P$	=	discretization point P
$y_{y,\mathrm{PW}}$	=	normal distance to the wall at the grid point closest to the wall
y^+	=	dimensionless wall distance
$\mathbf{\Delta}$	=	filter width
Δt	=	time step
δV_P	=	volume of Ω_P
ε_t	=	dissipation
γ	=	diffusion parameter
ρ	=	density
τ_w	=	wall shear stress
Ω_P	=	control volume centered around $\mathbf{x}_P$

Presented as Paper 2010-560 at the 48th AIAA Aerospace Sciences Meeting Including the New Horizons Forum and Aerospace Exposition, Orlando, Florida, 4–7 January 2010; received 7 March 2011; revision received 26 July 2012; accepted for publication 30 July 2012; published online 28 February 2013.

*Ph.D. Student, Department of Shipping and Marine Technology.
†Researcher, Defense and Security, Systems and Technology.
‡Associate Professor, Department of Shipping and Marine Technology. Member AIAA.
§Research Director, Defense and Security, Systems and Technology. Associate Fellow AIAA.

I. Introduction

FLOW-induced vibrations are of great importance in many engineering applications related to structural loads and fatigue, vibrations, human comfort, and fatigue, as well as noise. This concerns many diverse applications including ship appendages and propellers, buildings, bridges, offshore structures, and mooring cables. If the frequency content of the flow-induced vibrations coincides with the resonance frequency of, e.g., a building structure, this might have serious consequences. The most apparent engineering objectives is, hence, to reduce the negative impact of these flow structures to decrease unsteady wind loads of structures, to

extend the lifetime of the construction, and to reduce signature levels of submarines or noise levels from propellers for passenger and crew comfort. With better knowledge of the flow physics controlling this phenomena it might, however, also be possible to reduce the environmental impact by using lighter, or less, material or, e.g., in marine propeller design, to increase the efficiency of the propulsor. Accordingly, both the significance, as well as the complexity of flow-induced vibrations, make it an interesting and challenging subject of research.

The objective of this study is to provide a better understanding of these types of flows and give support in the validation of a fluid structure interaction methodology for complex engineering problems based on computational fluid dynamics (CFD). Accurate predictions of flows dominated by unsteady effects require a method that is able to correctly represent the key physical processes involved. Resolving all flow structures is possible for some academic cases, using direct numerical simulation (DNS), which, however, require exceptional computational resources, making DNS unfeasible for most engineering applications. More feasible for these types of flows are large-eddy simulation (LES) models in which the large (energetic) scales of motion are resolved while the effects of the small-scale turbulent structures are modeled. Concerning approaches based on Reynolds-averaged Navier–Stokes (RANS) equations, where one seeks the solution to the average flowfield and all fluctuations are modeled, the reliability can be questioned because available turbulence models are developed for steady flow conditions. In principle, this excludes all forms of hybrid RANS/LES models in which a RANS model is used in the boundary layer as the near-wall flow is unsteady here.

The flow around an oscillating cylinder constitutes a canonical case well suited for the understanding of unsteady loading and flow separation around bluff bodies and has previously been studied both experimentally [1–8] and numerically [9–11]. We will here perform LES of the experiments carried out in [3] including streamwise sinusoidal oscillations at two different frequency ratios, $f_e/f_0 = 0.44$ and 1.0, where f_e is the frequency by which the cylinder oscillates, and f_0 is the von Kármán shedding frequency. The simulations will be used to describe the flow development during one characteristic oscillation cycle, and the unsteady loading will be compared with the experimental results. Among previously performed computational studies of the case at the subharmonic frequency ratio, $f_e/f_0 = 0.44$, it was concluded in [9] that the two-dimensional LES was not capable of predicting the correct load, whereas the three-dimensional LES was sufficiently accurate to predict the load. We start by describing the computational model and the numerical methods used and validate our approach against experimental and DNS data for a fixed cylinder at $Re = 3900$. Next, we describe the experimental setup of the oscillating cylinder [3] and discuss the differences between the experimental and computational configurations. We then describe the different flow structures developing during one characteristic oscillation cycle and discuss how these differ at the two frequencies studied, as well as compare the predicted forces on the cylinder with the measured ones, prior to us ending with some concluding remarks.

II. Computational Flow Models

The computational flow model consists of the incompressible Navier–Stokes equations, which are extended to handle moving grids, comprising the balance equations of mass and momentum for a linear viscous fluid, e.g., [12]:

$$\partial_t(\mathbf{v}) + \nabla \cdot (\mathbf{v} \otimes (\mathbf{v} - \mathbf{v}_\mathrm{m})) = -\nabla p + \nabla \cdot \mathbf{S}, \qquad \nabla \cdot \mathbf{v} = 0 \quad (1)$$

where $\mathbf{v}$ is the velocity, $\mathbf{v}_\mathrm{m}$ is the grid velocity, p is the pressure, $\mathbf{S} = 2\nu\mathbf{D}$ is the viscous stress tensor, $\mathbf{D} = \frac{1}{2}(\nabla\mathbf{v} + \nabla\mathbf{v}^T)$ is the rate-of-strain tensor, and v is the viscosity. Most turbulent flows consist of vortex filaments and sheets with characteristic scales on the order of the Taylor and Kolmogorov scales, ℓ_T and ℓ_K, respectively, typically being orders of magnitude smaller than the integral scales, ℓ_I. In DNS [13] all flow scales (down to ℓ_K) are resolved making such simulations too expensive for engineering applications. Instead LES [14–17] in which all of the flow scales smaller than $\sim\ell_T$ are modeled, thus, having weaker resolution requirements, have emerged as a viable alternative for engineering predictions. RANS models [18] on the other hand do not have any physical resolution requirement; the properties of the turbulence model determine the grid size.

A. Large-Eddy Simulation

In LES, all scales larger than the grid spacing are resolved with a space/time accurate algorithm, and only the effects of the small, unresolved eddy scales need to be modeled. The LES equations are derived from Eq. (1) by low-pass filtering using a predefined filter kernel $G = G(\mathbf{x}, \boldsymbol{\Delta})$ in which Δ is the filter width so that

$$\partial_t(\bar{\mathbf{v}}) + \nabla \cdot (\bar{\mathbf{v}} \otimes (\bar{\mathbf{v}} - \mathbf{v}_\mathrm{m})) = -\nabla \bar{p} + \nabla \cdot (\nu \nabla \bar{\mathbf{v}} - \mathbf{B}) + \mathbf{m},$$
$$\nabla \cdot \bar{\mathbf{v}} = \mathrm{m} \quad (2)$$

where overbars denote the low-pass filtered dependent variables. The additional term separating Eq. (2) from Eq. (1) is the subgrid stress tensor $\mathbf{B} = (\overline{\mathbf{v} \otimes \mathbf{v}} - \bar{\mathbf{v}} \otimes \bar{\mathbf{v}})$, which is representing the influence of the small, unresolved scales on the large, resolved scales, and the commutation error terms, $\mathbf{m} = \overline{\nabla \cdot (\mathbf{v} \otimes \mathbf{v} + p\mathbf{I} - \mathbf{S})} - \nabla \cdot (\bar{\mathbf{v}} \otimes \bar{\mathbf{v}} + \bar{p}\mathbf{I} - \bar{\mathbf{S}})$ and $m = \nabla \cdot \bar{\mathbf{v}} - \overline{\nabla \cdot \mathbf{v}}$, are resulting from changing the order between differentiation and filtering. Although both terms contribute to the LES closure problem we here neglect $\mathbf{m}$, and focus the modeling effort on $\mathbf{B}$.

Modern explicit LES closures can broadly be classified as functional or structural models [14]. *Functional models* are designed to mimic the kinetic energy cascade from large to small scales that are considered a "universal" physical mechanism in fully developed turbulent flows. The main effect of the energy cascade is the energy drain at the resolved scales by the subgrid scales, $\varepsilon_t = -\mathbf{B} \cdot \bar{\mathbf{D}}$. An empirical model for ε_t is the use of a subgrid viscosity, ν_k; the amplitude of which is calibrated to enforce the desired mean energy cascade rate. The resulting contribution to the LES equations, Eq. (2), then becomes $\mathbf{B} \approx -2\nu_k \bar{\mathbf{D}}_D$. To close these models the subgrid viscosity, ν_k, needs to be prescribed by a model of the form $\nu_k = \ell_k v_k'$, where ℓ_k is the subgrid length scale, and v_k' is the subgrid velocity. A number of subgrid viscosity models are available [14] for a comprehensive review including the Smagorinsky model [19], the structure function model [20], the one equation eddy viscosity (OEEVM) model [21], and various dynamic versions of the models above [22,23]. *Structural models*, on the other hand, are designed to retain as much as possible of the overall structure of the true subgrid flux tensor and flux vectors. The first model of this kind was the scale-similarity (SS) model in [24] in which $\mathbf{B} \approx \overline{\bar{\mathbf{v}} \otimes \bar{\mathbf{v}}} - \bar{\bar{\mathbf{v}}} \otimes \bar{\bar{\mathbf{v}}}$. Although showing high correlations with data [25] this model is of restricted use for LES, because it does not have enough dissipation. However, by combining the SS model with a dissipative subgrid viscosity model, the mixed model $\mathbf{B} \approx \overline{\bar{\mathbf{v}} \otimes \bar{\mathbf{v}}} - \bar{\bar{\mathbf{v}}} \otimes \bar{\bar{\mathbf{v}}} - 2\nu_k \bar{\mathbf{D}}_D$ is obtained. Based on previous experience we combine the SS term with the OEEVM model [26], where $\nu_k - c_k \Delta k^{1/2}$ in which the subgrid kinetic energy, k, is estimated by solving a separate modeled transport equation of the form

$$\partial_t(k) + \nabla \cdot (k(\bar{\mathbf{v}} - \mathbf{v}_\mathrm{m})) = 2\nu_k \|\bar{\mathbf{D}}\|^2 + \nabla \cdot (\nu_k \nabla k) - c_\varepsilon k^{3/2}/\Delta \quad (3)$$

in which $c_k \approx 0.07$ and $c_\varepsilon \approx 1.05$ are model coefficients that are obtained by integrating the energy spectra [2].

B. Numerical Methods for Large-Eddy Simulation

Here we use OpenFOAM, [27], which is based on an unstructured collocated finite volume method in which the discretization uses Gauss theorem together with a multistep time-integration method [28]. The resulting discretized mass and momentum equations, respectively, take the form

$$\begin{cases} \frac{\beta_i \Delta t}{\delta V_P} \Sigma_f (\bar{\mathbf{v}} \cdot d\mathbf{A})_f^{n+1} = 0 \\ \Sigma_{i=0}^{\mathrm{m}} \left(\alpha_i (\bar{\mathbf{v}})_P^{n+i} + \frac{\beta_i \Delta t}{\delta V_P} \Sigma_f [((\bar{\mathbf{v}}_f - \mathbf{v}_\mathrm{m}) \cdot d\mathbf{A}_f) \bar{\mathbf{v}}_f) - (\nu + \nu_k)_f (\nabla \bar{\mathbf{v}})_f d\mathbf{A}_f]^{n+i} \right) = -\beta_i (\nabla \bar{p})_P^{n+i} \Delta t \end{cases} \tag{4}$$

in which $\mathbf{v}_P = \frac{1}{\delta V_P} \int_{\Omega_P} \mathbf{v} \, \mathrm{d}V$ defines the discrete representation of $\mathbf{v}$ for each control volume Ω_P concentrated around the point $\mathbf{x}_P$ with δV_P being the control volume of Ω_P; $d\mathbf{A}_f$ being the area of the cell face, f, of control volume Ω_P; Δt being the time step; and α_i and β_i being coefficients of the time integration scheme. More specifically, the time integration is here performed by a semi-implicit second-order two-point backward differencing scheme, where $\mathrm{m} = 2$, $\alpha_0 = 0.5$, $\alpha_1 = -2$, $\alpha_2 = 1.5$, $\beta_0 = \beta_1 = 0$, and $\beta_2 = 1.0$, whereas the convective fluxes, $\bar{\mathbf{v}}_f$, are approximated by linear interpolation between adjacent control volumes. The velocity gradient, $\nabla(\bar{\mathbf{v}})_f$, is decomposed into orthogonal and nonorthogonal parts to minimize the nonorthogonality error. Central difference approximations are applied to the orthogonal part, whereas face interpolation of the gradients of the dependent variables is used for the nonorthogonal parts. A Poisson equation is used to handle the pressure–velocity coupling, and it is solved using the pressure implicit with the splitting of operators procedure with a modified Rhie–Chow interpolation for cell-centered data [29]. The equations are solved sequentially with iteration over the explicit source terms to obtain fast convergence.

When a moving or deforming computational grid is used the temporal derivatives introduce a rate of change of the cell volume and a mesh motion flux due to the mesh convection. The relationship between the temporal derivative and the change in cell volume must satisfy the space conservation law, $\partial_t \int_V (\mathbf{v}) \, \mathrm{d}V = \int_S (\mathbf{v}_\mathrm{m} \cdot \mathbf{n}) \, \mathrm{d}S$, [30], in order to conserve mass. The change in cell volume is calculated from the sum of the mesh motion fluxes, $\Sigma_f (\mathbf{v}_\mathrm{m} \cdot \mathbf{n})_f$, during the current time step rather than from the grid velocity, $\mathbf{v}_\mathrm{m}$, making it consistent with the cell volume calculation. Here, the mesh points on the wall of the cylinder are calculated explicitly according to the sinusoidal motion of the cylinder, and the resulting mesh deformation is accounted for using a Laplace equation, $\nabla \cdot (\gamma \nabla \mathbf{v}_\mathrm{m}) = 0$, where γ is a diffusion parameter controlling the displacements of the grid points.

C. Wall Modeling for Large-Eddy Simulation

If the computational grid is too coarse to resolve the flow in the wall boundary layer, which is likely to be the case in most engineering flows, a model must be used to account for the presence of the wall. Such models are usually based on statistical arguments together with the mean velocity profiles of the viscous sublayer and the logarithmic region [18]. The majority of these methods need the mean wall shear stress, $\langle \tau_w \rangle$, to be specified, which may be complicated. As suggested in [31], more versatile methods, capable of seamlessly handling unstructured grids and complex geometries, can be developed from the filtered boundary-layer equations. Through simplification of these by assuming zero streamwise pressure gradient and convective transport they integrate analytically to the logarithmic law of the wall. This relation can be used to modify the subgrid model by adding a subgrid wall viscosity, ν_BC, to ν on the wall, so that the effective viscosity, $\nu + \nu_\mathrm{BC}$, becomes $\nu + \nu_\mathrm{BC} = \tau_w / (\partial v_y / \partial y)_\mathrm{PW} = u_\tau y_{y,\mathrm{PW}} / v_{y,\mathrm{PW}}^+$ where u_τ is the friction velocity, $y_{y,\mathrm{PW}}$ is the normal distance to the wall, $v_{y,\mathrm{PW}}^+$ is the dimensionless velocity, and the subscript PW denotes evaluation at the first grid point away from the wall. This wall model can be combined with any (explicit or implicit) subgrid model. To indicate that the wall model is used "+WM" is added to the name of the corresponding LES subgrid.

III. Validation of the Computational Model

The computational methodology used in this study, as described above, has been used extensively to examine a wide range of flows, providing a reference to current capabilities. The applications include fundamental cases, such as the Taylor–Green flow [32], homogeneous isotropic turbulence at the different Reynolds numbers [33], and fully developed turbulent channel flow at the friction velocity-based Reynolds numbers between 180 and 2000 [31]. Belonging to the category of more advanced cases are the flow over a contoured ramp [34], the flow over a surface-mounted 3-D hill [35], the flow past torpedo-like axisymmetric hulls [36], the flow past a prolate spheroid [37,38], flows around submarine and ship hulls [39,40], and low-speed and high-speed reacting flows [41–43]. However, as a first step toward quantifying the accuracy of the computational setup of the oscillating cylinder case, LES predictions of the flow past a fixed cylinder at $Re = v_0 D / \nu = 3900$ are here presented. Defining the case is the diameter, $D = 0.0143$ m, and the freestream velocity, $v_0 = 4.09$ m/s. The flow is examined using explicit LES on two different grids with the simulations summarized in Table 1.

The computational domain, which was the same for both the fixed and oscillating cylinder, is shown in Fig. 1a. The domain is rectangular shaped and measures $29D$ in the streamwise direction, $19D$ in the lateral direction, and $5D$ in the spanwise direction with the cylinder horizontally centered $9.5D$ downstream of the inlet. The corresponding grids are constructed using a block structured H grid with an O grid of radius $2.5D$ around the cylinder, see Fig. 1b. At the inlet, a Dirichlet condition is used for the velocity with $\bar{\mathbf{v}} - v_0 \mathbf{n}$, and a zero Neumann condition is used for the pressure, where $\mathbf{n}$ is the inward normal. At the outlet zero Neumann conditions are used for the velocity and the Dirichlet condition for the pressure, $\bar{p} = p_0$. At the top, bottom, and sides symmetrical conditions are used whereas no-slip conditions are applied to the cylinder. The initial condition used was a uniform flow, and in each case the sampling was initialized after the simulation was considered to have reached a fully developed state corresponding to $t > 29D / v_0$.

In Fig. 2, the flow around a circular cylinder is shown in terms of isosurfaces of the second invariant of the velocity gradient, revealing the presences of a complex vortical pattern involving a wide range of flow scales. On the top of the cylinder a shear layer enclosing the cylinder is observed and can be seen to develop small-scale instabilities that grow in size with increasing azimuthal angle. Further downstream in the separated shear layer these instabilities merge and subsequently roll up into the spanwise Kelvin–Helmholz (KH) billows that dominate the near wake. However, this rollup occurs asymmetrically with respect to the centerline of the wake suggesting that the convective Bénard/von Kármán instability dominates the wake dynamics. The large spanwise KH vortices are shed off the cylinder as discrete spanwise rollers that are not connected to the cylinder or to each other. The recirculating cylinder wake consequently detaches periodically and is advected downstream in a sinusoidal pattern. The shedding typically occurs with a frequency of $f_0 \approx St \cdot v_0 / D$ in which the Strouhal number, St, is empirically shown to be between 0.20 and 0.22. The LES predictions presented here exhibit a Strouhal number of $St \approx 0.21$. Between pairs of recently detached spanwise KH vortices secondary longitudinal vortices develop in the braid regions. These longitudinal finger-like vortices develop due to a secondary instability that occurs once the spanwise vortices have completed their first rollup and can clearly be seen to entwine and distort the spanwise KH vortices by exchanging momentum and energy. This results in a distortion and weakening of the spanwise KH vortices increasing with the distance from the cylinder until they eventually break up and disappear. The

Table 1 Summary of validation simulations performed

Case	Grid (million cells)	x^+	y^+	$z+$	Angle of separation, deg
1.1	0.6	6	2	10	92
1.2	1.2	3	1	5	90

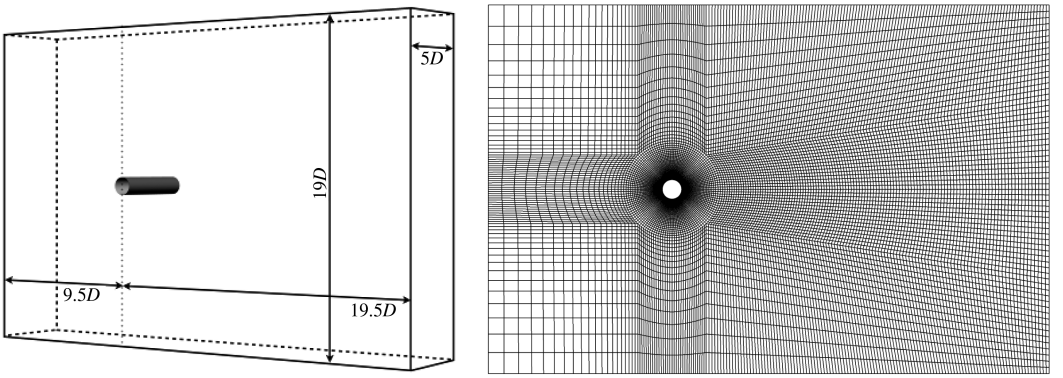

Fig. 1 Mesh description: a) computational domain; b) mesh topology.

longitudinal vortices on the other hand gain energy although becoming more and more distorted. Far downstream the wake is dominated by a topologically very complicated vorticity pattern, making it difficult to identify individual vortices.

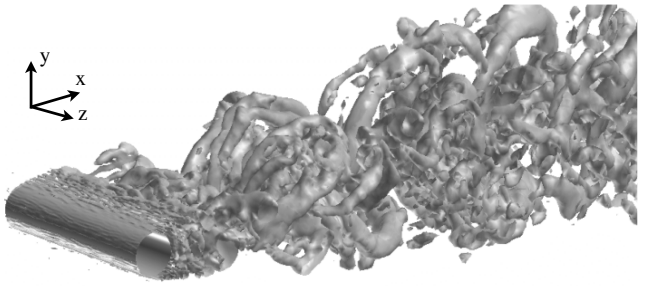

Fig. 2 Perspective view of flow past a circular cylinder in steady flow at $Re = 3900$ in terms of isosurfaces of the second invariant of the velocity gradient (= − 2e4).

In Fig. 3, results from the LES listed in Table 2 are presented together with the experimental data in [44–46] and the DNS results in [47]. In Fig. 3a, the predicted mean velocity along the centerline is seen to be in reasonable agreement with the experimental data and the DNS results. We note that the recirculation length is slightly underpredicted on the coarse grid, whereas it is slightly overpredicted on the fine grid. However, further downstream of the cylinder, $x/D > 4$, all LES predictions coincide well with experimental data. A comparison among the predictions, the measurement data, and the DNS results across the wake, as in Figs. 3a–3c, suggest that the streamwise velocity profiles at $x/D = 1.06, 1.54, 2.02, 4, 7$, and 10 are in good agreement with each other but with the LES resulting in a marginally too wide wake and a slightly too long recirculation region. Regarding the axial root mean square (rms) velocity fluctuations in Fig. 3c we find good agreement for all cross sections. Moreover, the pressure coefficient on the cylinder shown in Fig. 3d gives satisfactory results for all simulations and is exceptionally good on the fine grid.

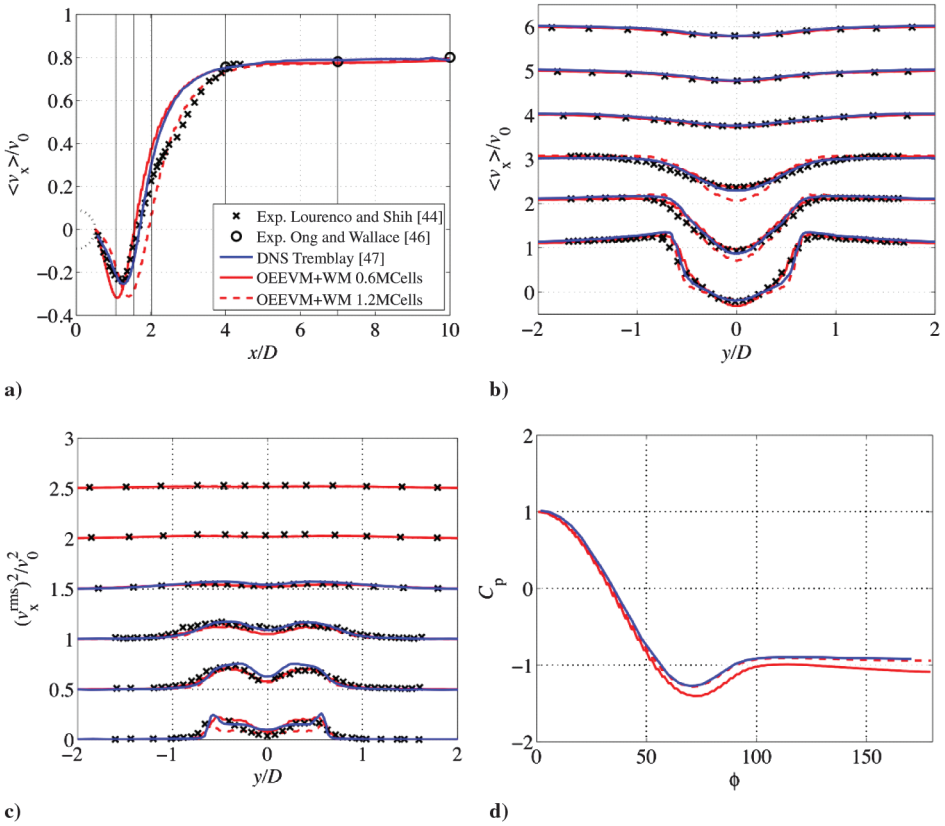

Fig. 3 Cylinder validation: a) mean velocity along centerline $y = 0$; b) streamwise velocity profiles; c) axial velocity rms fluctuations; d) pressure coefficient on the cylinder surface.

Table 2 Summary of oscillating cylinder simulations

Case	f_e/f_0	Grid (million cells)	y^+
2.1	1.00 (1st mode)	0.6	2
2.2	1.00 (1st mode)	1.2	1
2.3	1.00 (2nd mode)	1.2	1
2.4	0.44	1.2	1

IV. Oscillating Cylinder Experiments

Following the discussion in Sec. III we now turn to the flow past a circular cylinder undergoing streamwise sinusoidal oscillations. This case was experimentally studied in [1–3] using the recirculating, free-surface water channel at Lehigh University Fluid Mechanics Laboratory in Pennsylvania. The main test section of the channel has a width of 0.927 m, a depth of 0.610 m, and a length of 4.928 m. The experimental apparatus consisted of a cantilevered cylinder with length $L = 0.311$ m and diameter $D = 0.0254$ m oriented across the flow as seen in Fig. 4. The drag and lift forces on the cylinder were simultaneously acquired together with the corresponding flow-field using a strain gauge and high-image-density particle image velocimetry (HID-PIV). Different levels of submergence were tested, and the cases studied were characterized by the dimensionless excitation frequency, f_e/f_0, and the ratio, h_0/D, where f_0 is the von Kármán shedding frequency, f_e is the frequency by which the cylinder oscillates, and h_0 is the vertical distance from the free surface down to the center of the cylinder. For the completely submerged cases from which we chose the cases studied in this paper the water depth was 0.543 m and the cylinder located at $h_0/D = 11.73$. Moreover, the parameters controlling the streamwise sinusoidal displacement of the cylinder were kept constant, i.e., with a frequency of $f_e = 0.28$ Hz and an amplitude of $A = 0.96D$. Then, for each desired ratio, f_e/f_0, the experimentally determined Strouhal number of $St = f_0 D/v_0 \approx 0.2$ is used to determine the freestream velocity, v_0. In total, 14 cases in the range of $0.37 \leq f_e \leq 2.27$ were investigated, corresponding to $0.016 \leq v_0 \leq 0.095$ m/s and $405 \leq Re \leq 2482$. One remarkable case is when the cylinder oscillates at the fundamental of the von Kármán frequency, i.e., $f_e/f_0 = 1.00$. At this frequency, two different locked-on states were experimentally observed. The first mode, having alternating separation patterns, exhibits apparent variations in the lift force, see Fig. 5a. The second mode, on the other hand, possesses symmetrical separation resulting in a cancellation in the lift force and is less stable, see Fig. 5b. Two different locked-on states are indeed also found in the simulations performed, but the understanding of how and when they occur and the relationship between them lie out of the scoop of this study and for that reason only the first mode will be discussed further.

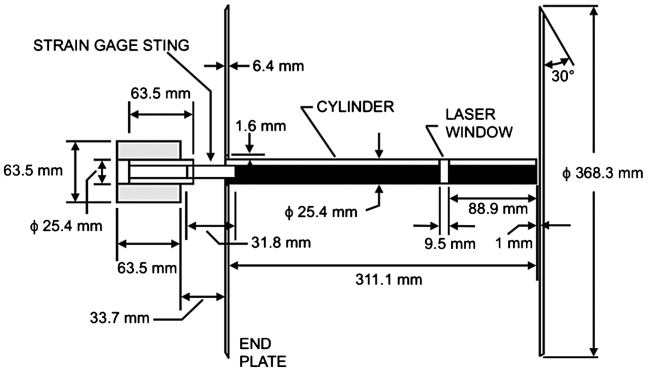

Fig. 4 Experimental setup used in [3]. (Published with the permission of the author.)

The transient drag coefficient, C_x, and lift force coefficient, C_y, is typically presented [1–3] using plots of force versus time, Fourier spectra, and Lissajous curves. Here C_x and C_y are defined as $C_x = F_x/(1/2\rho\hat{v}_c^2 LD)$ and $C_y = F_y/(1/2\rho\hat{v}_c^2 LD)$ with F_x and F_y being the drag and lift force, respectively; ρ being the density; and $\hat{v}_c = 2\pi f_e A$ being the maximum velocity of the cylinder. Figure 6 illustrates an example of how the time varying forces are presented with C_y on the vertical axis and time, t, on the horizontal axis. Out of the 102 cycles displayed 12.5 cycles were chosen, the window indicated by the two dashed lines, and presented using Lissajous curves. Moreover, a more detailed investigation was performed for $f_e/f_0 = 0.44$ and 1.00 correlating the time varying transverse force coefficient, C_y, with instantaneous vorticity patterns provided by the HID-PIV.

The experimental setup differs from an idealized (computational) configuration in a number of ways: for example the presence of the water surface, the gravitation, and the presence of the channel bottom. Moreover, the correct reconstruction of the sinusoidal displacement, $x_c = A\cos(2\pi f_e)$, becomes evidently important in the Lissajous curves. A deviation from the real cylinder period by less than a hundredth of a second will result in a growing time lag between the displacement and the measured force. The influence of this time lag on the shape of the Lissajous curves is apparent in the plots in Figs. 7a and 7b, where two different frequencies are used to plot approximately 100 cylinder oscillations during a time of 360 s.

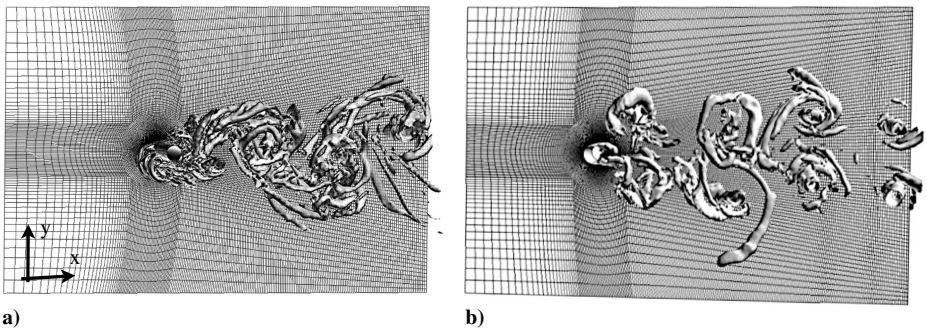

a) b)

Fig. 5 Isosurface of the second invariant of the velocity gradient (= − 0.2) with $f_e/f_0 = 1.00$: a) first mode and b) second mode.

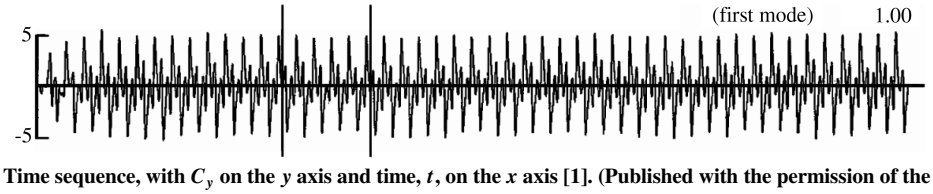

Fig. 6 Time sequence, with C_y on the y axis and time, t, on the x axis [1]. (Published with the permission of the author.)

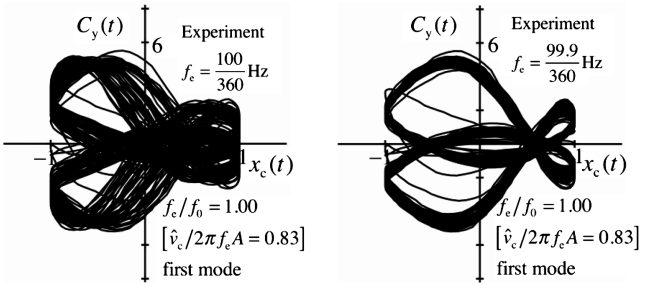

a) b)

Fig. 7 Example of Lissajous curves emphasizing the sensitivity of these graphs to f_e: a) $f_e = 100/360$ Hz and b) $f_e = 99.9/360$ Hz. (Experimental data provided in [3].)

Ongoren and Rockwell [1], Williamson and Roshko [2], and Cetiner and Rockwell [3] stated a truly locked-on state is acquired for $f_e/f_0 = 1.00$. This lock-on state should be visible as persistent curves in the Lissajous curves, which apparently is not the case in Fig. 7a. However, by prescribing a frequency of $f_e = 99.9/360$ Hz a truly locked-on state can be achieved as seen in Fig. 7b. Because the discrepancy increases with time effort has been made to use data from early oscillations. With the experimental results presented and provided by Cetiner [5], in terms of time histories of C_x and C_y, they have, by the authors of this paper, been postprocessed in the same manner as the LES results.

V. Flow Physics and Validation

Here we will discuss LES predictions of the flow around the oscillating cylinder. Drag and lift forces from LES will be compared with experimental data provided in [3]. In this study two grids of 0.6 and 1.2 MCells are used with the same type of boundary conditions and topology of the computational domain as for the fixed cylinder, see Sec. II. Moreover, the initial conditions were a uniform flow, and each simulation needed approximately 10 oscillations to reach the locked-on state. Because the mesh is moving the diffusion term in the dynamic mesh deformation equations is needs to be defined; here it is set to $\gamma = 1/\ell^2$, where ℓ is the distance to the wall giving little or no mesh deformation in the cylinder near wall region. In all of the simulations the presence of a free surface, bottom wall, and gravitation is neglected. Moreover, the cylinder diameter and the amplitude and frequency by which the cylinder oscillates were set according to the corresponding experimental setup, i.e., $D = 0.0254$, $f_e = 0.28$ Hz, and $A = 0.96D$. Additional parameters were determined as described in Sec. IV. In Table 2 a summary of the simulations performed is presented. Although we have performed simulations using two different grids we concentrate on the fine grid LES results to simplify the discussion.

We base our discussion of the flow physics on one characteristic oscillation for the two cases $f_e/f_0 = 1.00$ and $f_e/f_0 = 0.44$, respectively. The aim is to correlate the loading of the cylinder with phenomena observed in the flow. First, we consider case 2.2 when the cylinder oscillates at the von Kármán shedding frequency, $f_e/f_0 = 1.00$ (first mode), as shown in Fig. 8. Following that, we continue

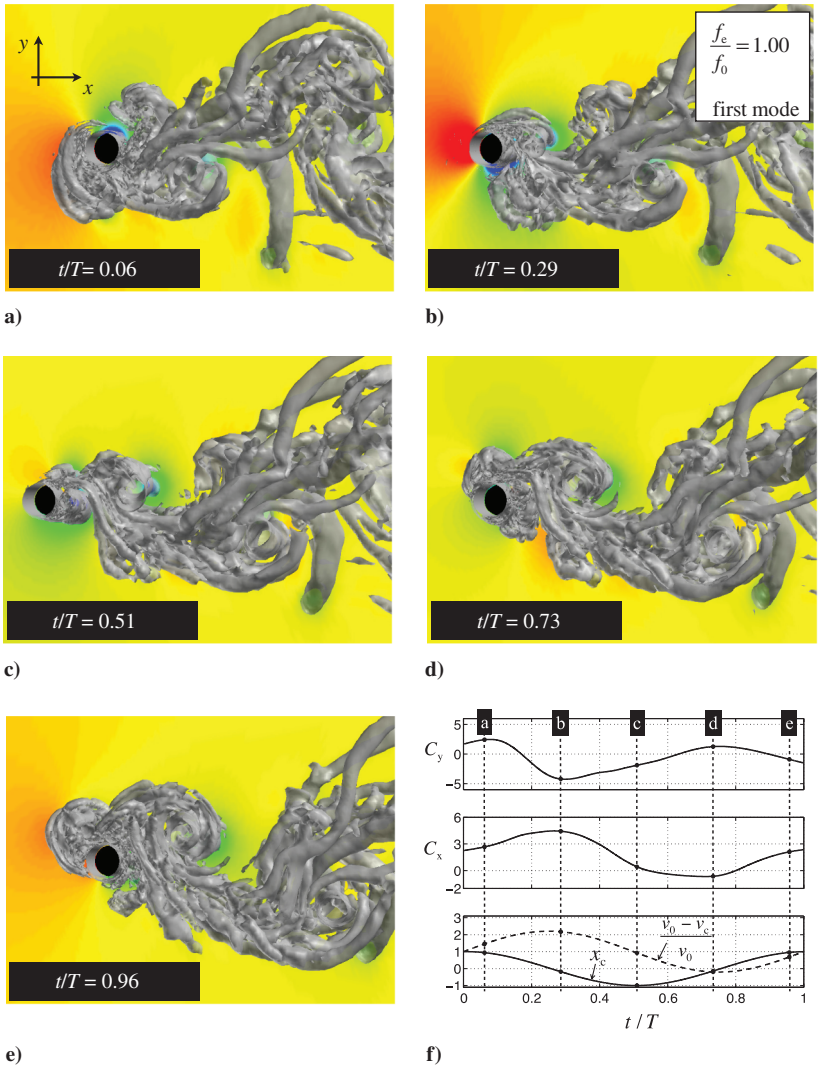

Fig. 8 Iso-surfaces of the second invariant of the velocity gradient (= − 0.2) together with plots of displacement, force coefficients and relative velocity during one characteristic cylinder cycle of case 2.2.

with case 2.4 when the cylinder oscillates at the subharmonic frequency $f_e/f_0 = 0.44$, as shown in Fig. 9. In both cases, the flow is visualized using isosurfaces of the second invariant of the velocity gradient, which is representative of coherent vortex structures; the instantaneous pressure field, p; and correlated with the normalized displacement of the cylinder, x_c; the normalized relative velocity, $(v_0 - v_c)/v_0$; and the total drag and lift force coefficients, C_x, and C_y, respectively. Here, the velocity of the cylinder is denoted by v_c. The reduction in grid size between case 2.2 and case 2.1 results in slightly reduced lift and drag forces but without any visible changes in the flow physics.

For case 2.2, Fig. 8a shows the cylinder shortly after leaving its most downstream position, whereafter it moves past the midposition in Fig. 8b to reach the most upstream position in Fig. 8c. Next, in Fig. 8d, the cylinder once again crosses the midposition, and finally in Fig. 8e it ends up just prior to the turn and close to the location where it started in Fig. 8a. In Fig. 8f, the drag and lift force coefficients are correlated with the relative velocity and the motion of the cylinder. Only one cylinder oscillation is considered here even though a full cycle spans over two complete cylinder oscillations. This is sufficient due to the alternating flowfield, which is mirrored around the horizontal centerline. Thus, the following cylinder oscillation results in the corresponding forces but with opposite sign in the lift force. The drag force and the relative velocity are more or less linearly dependent, cf., Fig. 8f, and, hence, a maximum value in the relative velocity implies a maximum value in the drag force. At the instant represented in Fig. 8a the relative velocity is marginally higher than the mean relative velocity during one oscillation, and a large collection of vortical structures can be observed behind, in front of, and at the lower half of the cylinder. The corresponding low-pressure region on the upper half of the cylinder results in a locally higher velocity and a positive lift force, forcing the flow structures ahead past the top of cylinder. From this condition, an alternating vortex shedding originates as observed when the cylinder attains the midpoint position in Fig. 8b. At that position, a low-pressure region at the bottom of the cylinder combined with a large vortex sheet at the top of the cylinder results in a minimum in the lift force. Moreover, due to a maximum in relative velocity the drag force attains a maximum value. In Fig. 8c the cylinder turns and starts moving with the freestream. The observed asymmetry, with a low-pressure region related to a vortex shed from the lower surface and a smaller vortex developing on the upper surface of the cylinder, results in a negative lift force. From here the cylinder moves downstream from Figs. 8c to 8d. The movement leads to an interruption in the periodic shedding induced when the cylinder moved upstream, and the vortex on the top of the cylinder is pushed away. This, together with the internal momentum already induced in the fluid, creates a large cloud of small-scale vortices seen in the region close to the top of the cylinder in Fig. 8e. The cylinder movement from the midposition in Fig. 8d close to the most upstream position in Fig. 8e changes the lift force from a positive to a negative value. This behavior is then repeated by the following oscillation but mirrored in the centerline.

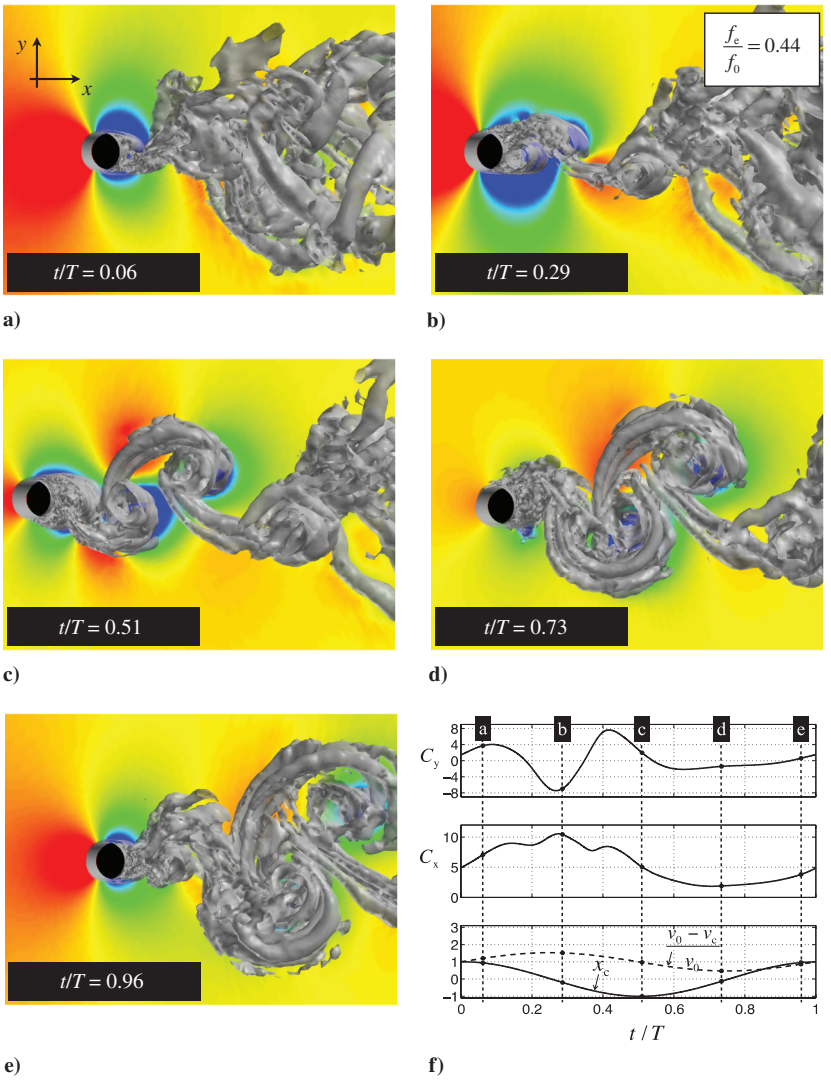

Fig. 9 Iso-surfaces of the second invariant of the velocity gradient (= − 0.2) together with plots of displacement, force coefficients and relative velocity during one characteristic cylinder cycle of case 2.4.

In Fig. 9, the corresponding sequence is shown for the subharmonic frequency of case 2.4. In Fig. 9a, the cylinder has just turned and is close to its most downstream position, whereafter it passes the midposition in Fig. 9b to reach the most upstream position in Fig. 9c. Subsequently, in Fig. 9d, the cylinder crosses its midposition to finally, in Fig. 9e, end up close to where it originated in Fig. 9a just prior to the turn. Case 2.4 does not exhibit a truly locked-on state, which means that the cylinder oscillation shown is a sample of a much longer cycle. One evident consequence of the lower value of f_e/f_0 is that the shape of the drag force is modified in Fig. 9f between times a) and b) compared to Fig. 8f. The observed difference is due to a higher shedding frequency, which enables two vortices instead of just one to separate during the same amount of time. In Fig. 9a, the cylinder has already started to move toward the inlet, and as a result an alternating vortex shedding has been initiated. This is observed as an asymmetric pressure field and a vortex that separates at the upper part of the cylinder, resulting in a positive lift force. In Fig. 9b, the cylinder passes the midpoint position and reaches its maximum relative velocity and, thus, inflicts a maximum in the drag force. In addition, the state of the vortex shedding has shifted, giving a negative lift force as a result of a vortex shedding on the upper side of the cylinder. In Fig. 9c, the cylinder reaches its most upstream position, and the relative velocity once again attains its mean value. Here, the spanwise longitudinal vortices, observed in the non-oscillating case, are visible and so are the longitudinal finger-like vortex structures connecting them. A relatively small lift force is the result of an almost symmetrical shedding pattern and pressure distribution around the cylinder. Subsequently, the cylinder starts to move downstream into its own wake encountering a cloud of flow structures slightly more concentrated at the top of the cylinder. The consequences seen in Fig. 9d are a small negative lift force with an almost symmetrical pressure distribution and a cloud of flow structures being pushed over the top of the cylinder. Furthermore, at this time the relative velocity of the cylinder attains a minimum, which is reflected as a minimum also in the drag force. In Fig. 9e, the cylinder has almost reached its most downstream position, and the relative velocity is close to its mean value.

A convenient way of presenting the time history of the unsteady loading is by means of Lissajous curves [48], describing the variations of C_x and C_y vs. x_ca and C_y vs. C_x. Using this approach repetitive patterns in the force response on the cylinder undergoing a sinusoidal motion can be demonstrated. One should, however, keep in mind the sensitivity of these plots when reconstructing the sinusoidal displacement, x_c, see Fig. 7, and the discussion in Sec. IV. In Figs. 10 and 11 we present the Lissajous curves from cases 2.2 and 2.4 with $f_e/f_0 = 1.00$ (first mode), and $f_e/f_0 = 0.44$, respectively. These curves are reconstructed using 9 out of 100 oscillations from the experiments and 9 out of 100 oscillations from the simulations. The upper panels represent the LES predictions, and the lower panels represent the experimental data. The primary characteristics of the experimental force traces are, in both cases 2.2 and 2.4, well captured by the LES computations including the general shape of the curves and the location of zero crossings but also the magnitude of the force components. There is also a pronounced spread in the forces similar to the experiments, demonstrating the unsteady nature of LES.

Figure 10 presents the Lissajous curves from the LES computations (upper panels) and from the experiments (lower panels) for case 2.2 ($f_e/f_0 = 1.00$). To facilitate the interpretation of these plots arrows have been added between the locations corresponding to Figs. 8b and 8c indicating the direction in time. Because the flow is alternating, two different arrows (solid and dashed) are used where the solid line is representing a separation at the top of the cylinder, and the dashed line is representing a separation at the bottom of the cylinder. The blue circle in Fig. 10 corresponds to Fig. 8a, and the red circles correspond to Figs. 8b–8e. Comparing the predicted and measured force distributions we find that the shapes are similar but with small deviations primarily in the magnitude of the forces. In general, we note that the LES underpredicts the forces by about 5% compared to the measurements. An exception, however, is the lift force, which gets overpredicted during the downstream movement of the cylinder. An interesting observation is that the spread of the Lissajous curves are larger for C_y in the LES predictions than for the experimental data, whereas for C_x the spread is larger in the experimental data than in the LES predictions. Moreover, the spread in the LES predictions is rather even throughout the cycle, whereas for the experiments the largest spread is observed in C_x at a location close to the midposition, cf., Figs. 10b and 10e. We also remark that the spread in the measured drag force is dominated by a persistent deviation between two following cycles indicated by the dashed and solid arrow in Fig. 10e. The larger value, the solid arrow, is related to a separation on the top of the cylinder, and the lower value corresponds to a separation on the bottom of the cylinder. Possible explanations for this asymmetry in the measurements and the differences between the predicted and measured force distributions include the influence of the free surface, gravity, the presence of the channel bottom, or an imperfectly manufactured or mounted cylinder.

In Fig. 11 we show the Fourier spectra of the lift force coefficient, C_y, for case 2.2. Comparing the measured and predicted spectra we find that the location of the spectral peaks coincide very well, that is at $f/f_e = 0.5$, 1.5, 2.5, and 3.5. Two major peaks are observed at $f/f_e = 0.5$ and 1.5. The peak at $f/f_e = 0.5$, moreover, reflects the fact that the cycle spans over two cylinder oscillations.

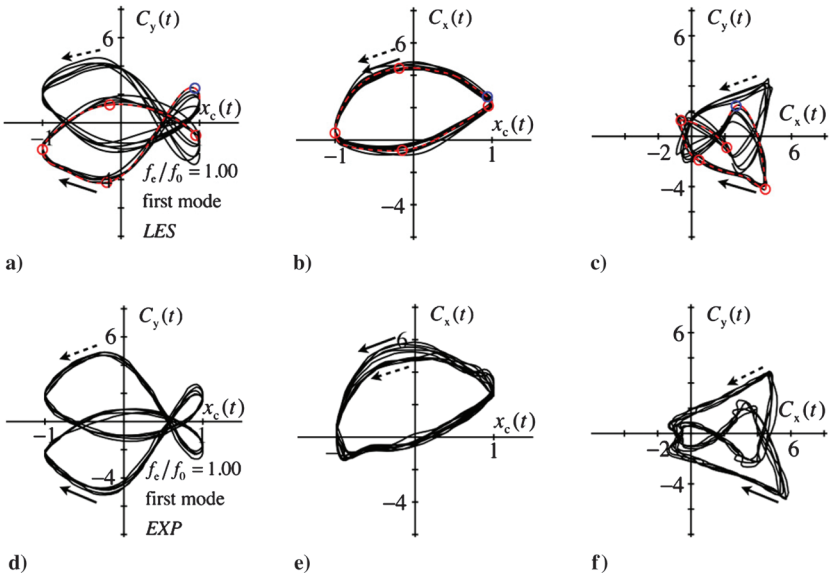

Fig. 10 Lissajous curves of lift force coefficient, drag force coefficient, and cylinder displacement. LES predictions in the upper panel and experimental data in the lower panel.

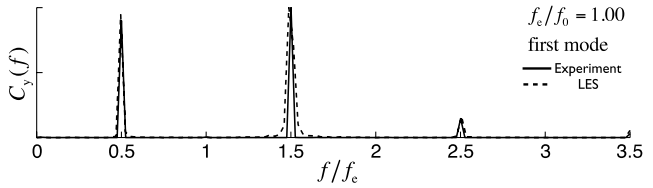

Fig. 11 Fourier spectra of the lift force coefficient, C_y, experiments are solid line, LES is dashed line.

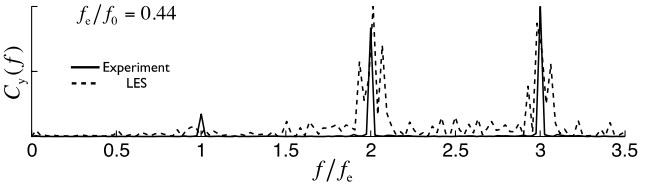

Fig. 13 Fourier spectrum of lift force coefficient, C_y, experiments are solid line, LES is dashed line.

Figure 12 presents the Lissajous curves from the LES computations (upper panels) and from the experiments (lower panels) for case 2.4 ($f_e/f_0 = 0.44$). To facilitate the interpretation of these plots arrows have been added between the locations corresponding to Figs. 9b and 9c indicating the direction in time. The blue circle in Fig. 12 corresponds to Fig. 9a, and the red circles correspond to Figs. 9b–9e. Comparing the predicted and measured force distributions we find that this case exhibits larger variations over a typical cycle than in case 2.2 ($f_e/f_0 = 1.00$) both in the experimental data and in the LES predictions. The overall agreement between the experiment and LES is, however, good. When comparing the two C_y curves it is clear that all zero crossings, local maxima, and local minima occur at approximately the same place. The discrepancies appear to be consistent with those observed for case 2.2, i.e., that the LES generally underpredicts the forces by about 5% compared to the measurements, whereas the predicted lift force related to a cylinder movement upstream tends to be somewhat too large. Moreover, the measured drag force related to a separation on the top of the cylinder results in a difference in magnitude in the two C_y curves; the same effect as seen for $f_e/f_0 = 1.00$. An interesting difference that is visible in the LES computations is the C_y curve, which alternates, i.e., it becomes reflected about the x axis. Shown here are only 9 out of 100 oscillations from the simulation and 9 out of 100 oscillations from the experimental trace, and the symmetry in the simulation becomes apparent when all cycles are plotted. This does not happen in the experiment and might be due to the completely symmetrical nature of the simulation compared to the experiment in which the fluid experiences different upper and lower blockage variations.

In Fig. 13 we show the Fourier spectra of the lift force coefficient, C_y, for case 2.4. The experimental spectra exhibits three distinct peaks at $f.f_e = 1, 2$, and 3. Peaks at these locations are also observed in the spectrum from the LES prediction. However, the predicted spectrum show three peaks centered at each of the experimentally

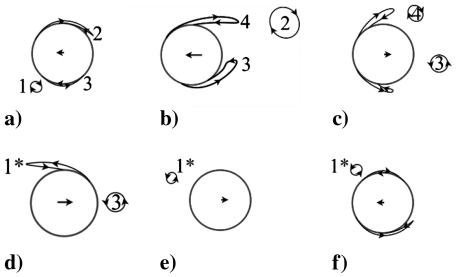

Fig. 14 Schematic pictures of the flow at the dimensionless frequency number $f_e/f_0 = 1.00$ (first mode) at times $t/T = 0.06, 0.29, 0.51, 0.73, 0.96$, and 1.06.

observed peaks. This might be a direct consequence of the alternating shedding observed in the LES simulations but not described in the experimental investigation.

Next, we will describe the creation, destruction, and movement of the major vortices governing the flow at the two oscillation frequencies, $f_e/f_0 = 1.00$ (first mode) shown in Fig. 14 and 0.44 shown in Fig. 15. This is done based on the findings from the Lissajour curves, Figs. 10 and 12, and are presented as schematic diagrams of vortices and shear layers of the flow. The panels a), b), c), d), e), and f) represent the times $t/T = 0.06, 0.29, 0.51, 0.73, 0.96$, and 1.06. To better keep track of where the vortices are created and how they travel along with the flow each vortex and its corresponding shear layer has been assigned with a number. Furthermore, an arrow has been added at the center of the cylinder to represent the cylinder velocity. Starting with $f_e/f_0 = 1.00$ (first mode) the sequence starts with the cylinder at the most downstream position in Fig. 14a, where an initial development of an alternating vortex shedding is observed. One vortex, 1, and two shear layers, one at the bottom, 3, and one slightly larger at the top of the cylinder, 2, are visible. The vortex

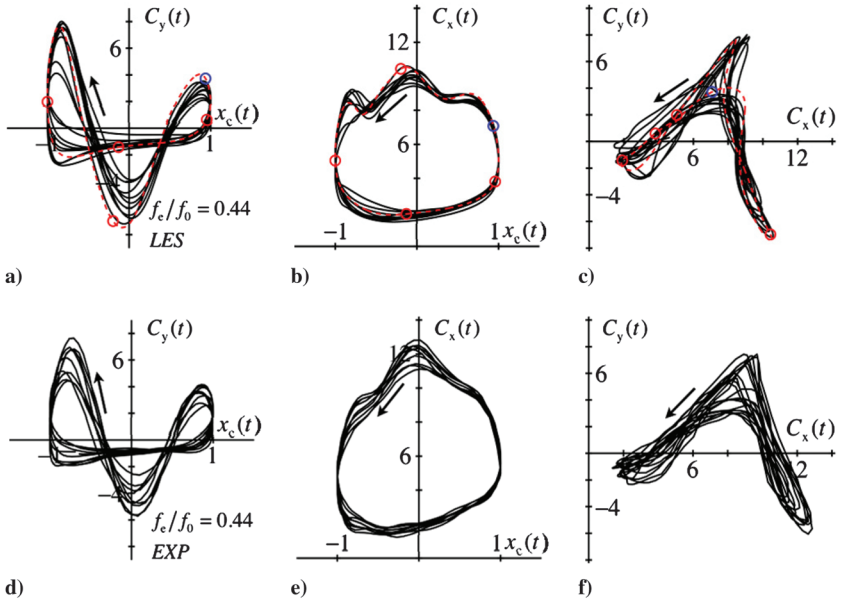

Fig. 12 Lissajous curves of transverse force, C_y, inline force, C_x, and cylinder displacement, x_c. LES predictions in upper panel and experimental data in lower panel. Arrows indicating direction in time.

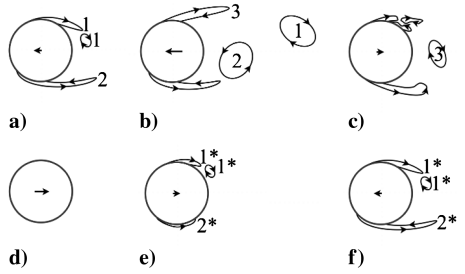

Fig. 15 Schematic pictures of the flow at the dimensionless frequency number $f_e/f_0 = 0.44$ at times $t/T = 0.06, 0.29, 0.51, 0.73, 0.96,$ and 1.06.

breaks up as it collides with the cylinder moving upstream, and the momentum from the vortex is transferred to the shear layer forming at the cylinder surface. The larger shear layer, 2, subsequently develops into a clockwise oriented vortex, which is visible downstream of the cylinder in Fig. 14b. In Fig. 14b, the two vortex sheets are still visible and are later on seen to develop into one vortex each. The first vortex, 3, at the bottom of the cylinder in Fig. 14c, moves with the freestream until it is caught up and totally diminished by the momentum of the cylinder between Figs. 14d and 14e. The second vortex, 4, is pushed away and passes over the cylinder out of frame in Fig. 14d. The acceleration of the cylinder downstream in Figs. 14c–14e creates a shear layer on the upper side that subsequently results in a small vortex, 1*. This smaller vortex, 1*, corresponds to the vortex, 1, visible in Fig. 14a, which in turn originates from the preceding downstream movement of the cylinder.

In Fig. 15, the corresponding schematic diagrams at $f_e/f_0 = 0.44$ are shown. In the first panel, Fig. 15a, the flowfield upstream and close to the cylinder mimics the underlying conditions that give rise to the alternating vortex shedding governing the von Kármán vortex street; one shear layer, 1, on the top of the cylinder with a corresponding vortex, 1, and one shear layer, 2, on the bottom of the cylinder. In Fig. 15b, a second vortex, 2, can be observed this time by shed from the shear layer, 2, at the lower part of the cylinder. The two vortices, both visible in Fig. 15b, move downstream and out of the picture in Fig. 15c. During the same time a third vortex, 3, is produced on the top of the cylinder, and due to the slowing down of the cylinder it is forced down behind it. In Fig. 15d, the third vortex, 3, has collided with and been scattered by the cylinder, and no apparent vortices are to be found. Prior to the turn, Fig. 15e, two new vortex sheets are developed: one, 1*, on the top with a corresponding vortex, 1*, and a second one, 2*, on the bottom of the cylinder. In Fig. 15f, similar conditions as in Fig. 15a have been reached representing the same location in the cylinder oscillation period as Fig. 15a.

VI. Conclusions

In this study large-eddy simulation (LES) was performed of the flow past a circular cylinder undergoing streamwise sinusoidal oscillations. The objectives of this investigation are to elucidate the flow physics involved in flow-induced vibrations and to study the predictive capabilities of LES for such flows, thereby, giving support in the validation of a fluid structure interaction methodology for complex engineering problems based on computational fluid dynamics (CFD). This is motivated by an increasing interest in reducing, e.g., unsteady loads of structures, the signature levels of navy vessels or noise levels from the propeller for passenger and crew comfort or to extend the lifetime of the construction, thus, giving a necessity of the tools able to predict these flows.

The flow around an oscillating cylinder was chosen as a first benchmark case due to the availability of high-quality experimental data and a simple geometrical body and well-defined motion. The experiments were obtained with a cantilevered cylinder in the free-surface water channel at Lehigh University Fluid Mechanics Laboratory. This flow exhibits many of the important flow phenomena, such as a von Kármán vortex street, Kelvin–Helmholtz instabilities, and the constantly changing relative velocity due to the oscillation, which results in a rich blend of vortices of different size. However, prior to the oscillating cylinder computations, the flow around a fixed cylinder was investigated using LES and validated against experimental data and a direct numerical simulation (DNS).

The LES results, both for the fixed and the oscillating cylinder, agree well with experimental data and, in the case of the fixed cylinder, previous LES and DNS predictions. By summarizing the predictions of the oscillating cylinder case a good agreement is seen with experimental drag and lift forces concerning both the general shape of the Lissajous curves used to describe the force variation, as well as the magnitude of these forces. This holds for both frequencies investigated, $f_e/f_0 = 1.00$ and $f_e/f_0 = 0.44$. However, in the first case of oscillation at the fundamental frequency, $f_e/f_0 = 1.00$, a larger spread was observed in the predicted lift force compared with the experimental, whereas for the drag force the experiments exhibited a larger spread. In the case of oscillation at the subharmonic frequency, $f_e/f_0 = 0.44$, an alternation was found of the locked-on state in the simulations. In other words, the vortex-separation pattern could shift completely, e.g., a repetitive separation originating from the top of the cylinder would after a few oscillations occur instead at the bottom, which is something that is not observed in the experimental data. It is believed that the alternation is due to the completely symmetrical nature of the simulation, whereas the experimental configuration includes some asymmetries due to e.g., gravitation. At both frequencies an apparent correlation was observed between extremum in the lift force and vortex separation.

Acknowledgments

The authors wish to acknowledge the financial support from Vinnova through the maritime competence center Lighthouse, the Swedish Armed Forces, and the Swedish Defense Material Agency. The computations were performed on C3SE computing resources. The authors wish to thank O. Cetiner for valuable input and for providing experimental data.

References

[1] Ongoren, A., and Rockwell, D., "Flow Structure from an Oscillating Cylinder Part 2. Mode Competition in the Near Wake," *Journal of Fluid Mechanics*, Vol. 191, 1988, pp. 225–245.

[2] Williamson, C. H. K., and Roshko, A., "Vortex Formation in the Wake of an Oscillating Cylinder," *Journal of Fluids and Structures*, Vol. 2, No. 4, 1988, pp. 355–381. doi:10.1016/S0889-9746(88)90058-8

[3] Cetiner, O., and Rockwell, D., "Streamwise Oscillations of a Cylinder in a Steady Current. Part 1. Locked-on States of Vortex Formation and Loading," *Journal of Fluid Mechanics*, Vol. 427, 2001, pp. 1–28.

[4] Cetiner, O., and Rockwell, D., "Streamwise Oscillations of a Cylinder in a Steady Current. Part 2. Free-Surface Effects on Vortex Formation and Loading," *Journal of Fluid Mechanics*, Vol. 427, 2001, pp. 29–59.

[5] Cetiner, O., "Flow Structure and Loading due to an Oscillating Cylinder in a Steady Current," Ph.D Dissertation, Dept. of Mechanical Engineering and Mechanics, Lehigh Univ., Bethlehem, Pennsylvania, 1998.

[6] Lee, T., "Investigation of Unsteady Boundary Layer Developed on a Rotationally Oscillating Circular Cylinder," *AIAA Journal*, Vol. 37, No. 3, 1999, pp. 328–336.

[7] Keun-Shik, C., and Jong-Youb, S., "Patterns of Vortex Shedding from an Oscillating Circular Cylinder," *AIAA Journal*, Vol. 30, No. 5, 1992, pp. 1331–1336.

[8] Jones, J. D., and Fuller, C. R., "Noise Control Characteristics of Synchrophasing. II—Experimental Investigation," *AIAA Journal*, Vol. 24, No. 8, 1986, pp. 1271–1276. doi:10.2514/3.9431

[9] Liefvendahl, M., and Lillberg, E., "Computational Methods for Unsteady Fluid Force Predictions Using Moving Mesh Large Eddy Simulations," AIAA Paper 2005-4144, 2005.

[10] Lu, X. Y., and Dalton, C., "Calculation of the Timing of Vortex Formation from an Oscillating Cylinder," *Journal of Fluids and Structures*, Vol. 10, No. 5, 1996, pp. 527–541. doi:10.1006/jfls.1996.0035

[11] Saritas, M., and Cetiner, O., "Flow Structure and Loading due to an Oscillating Cylinder in Steady Current," *Proceedings of the 7th International Symposium on Fluid Control, Measurement and Visualization*, Sorrento, Italy, 25–28 Aug. 2003.

[12] Pope, S. B., *Turbulent Flows*, Cambridge Univ. Press, Cambridge, England, U.K., 2000.
[13] Hsiao, C.-T., and Pauley, L., "Direct Numerical Simulation of Unsteady Finite-Span Hydrofoil Flow," *AIAA Journal*, Vol. 37, No. 5, 1999, pp. 529–536. doi:10.2514/2.759
[14] Sagaut, P., *Large Eddy Simulation for Incompressible Flows*, 3rd ed., Springer–Verlag, Berlin, 2006.
[15] Grinstein, F. F., Margolin, L., and Rider, B., *Implicit Large Eddy Simulation: Computing Turbulent Fluid Dynamics*, 1st ed., Cambridge Univ. Press, Cambridge, England, U.K., 2007.
[16] Lesieur, M., and Metais, O., "New Trends in Large Eddy Simulations of Turbulence," *Annual Review of Fluid Mechanics*, Vol. 28, 1996, pp. 45–82. doi:10.1146/annurev.fl.28.010196.000401
[17] Fureby, C., "Towards the use of Large Eddy Simulation in Engineering," *Progress in Aerospace Sciences*, Vol. 44, No. 6, 2008, pp. 381–396. doi:10.1016/j.paerosci.2008.07.003
[18] Wilcox, D. C., *Turbulence Modelling for CFD*, 3rd ed., DCW Industries, Inc., California, 2006.
[19] Smagorinsky, J., "General Circulation Experiments With the Primitive Equations I. The Basic Experiment," *Monthly Weather Review*, Vol. 91, No. 3, 1963, pp. 99–164. doi:10.1175/1520-0493(1963)091<0099:GCEWTP>2.3.CO;2
[20] Metais, O., and Lesieur, M., "Spectral Large Eddy Simulation of Isotropic and Stably Stratified Turbulence," *Journal of Fluid Mechanics*, Vol. 239, 1992, pp. 157–194. doi:10.1017/S0022112092004361
[21] Schumann, U., "Subgrid Scale Model for Finite Difference Simulation of Turbulent Flows in Plane Channels and Annuli," *Journal of Computational Physics*, Vol. 18, No. 4, 1975, pp. 376–404.
[22] Germano, M., Piomelli, U., Moin, P., and Cabot, W. H., "A Dynamic Subgrid-Scale Eddy Viscosity Model," *Physics of Fluids*, Vol. 3, No. 7, 1994, pp. 1760–1765.
[23] Menon, S., and Kim, W.-W., "High Reynolds Number Flow Simulations Using the Localized Dynamic Subgrid-Scale Model," AIAA Paper 1996-425, 1996.
[24] Bardina, J., Ferziger, J. H., and Reynolds, W. C., "Improved Subgrid-Scale Models for Large-Eddy Simulations," AIAA Paper 1980-1357, 1980.
[25] Liu, S., Meneveau, C., and Katz, J., "On the Properties of Similarity Subgrid-Scale Models as Deduced from Measurements in a Turbulent Jet," *Journal of Fluid Mechanics*, Vol. 275, 1994, pp. 83–119. doi:10.1017/S0022112094002296
[26] Bensow, R. E., and Fureby, C., "On the Justification and Extension of Mixed Models in LES," *Journal of Turbulence*, Vol. 8, No. 54, 2007.
[27] Weller, H. G., Tabor, G., Jasak, H., and Fureby, C., "A Tensorial Approach to Computational Continuum Mechanics Using Object Oriented Techniques," *Computers in Physics*, Vol. 12, No. 6, 1998, pp. 620–631. doi:10.1063/1.168744
[28] Lambert, J. D., *Computational Methods in Ordinary Differential Equations*, 1st ed., Wiley, New York, 1973.
[29] Rhie, C. M., and Chow, W. L., "Numerical Study of the Turbulent Flow Past an Airfoil with Trailing Edge Separation," *AIAA Journal*, Vol. 21, No. 11, 1983, pp. 1525–1532. doi:10.2514/3.8284
[30] Demirdzic, I., and Peric, M., "Space Conservation Law in Finite Volume Calculations of Fluid Flow," *International Journal for Numerical Methods in Fluids*, Vol. 8, No. 9, 1988, pp. 1037–1050. doi:10.1002/(ISSN)1097-0363
[31] Fureby, C., "On LES and DES of Wall Bounded Flows," *Ercoftac Bulletin*, March 2007.
[32] Drikakis, D., Fureby, C., Grinstein, F. F., and Youngs, D., "Simulations of Transition and Turbulence Decay in the Taylor-Green Vortex," *Journal of Turbulence*, Vol. 8, No. 20, 2007.
[33] Fureby, C., Tabor, G., Weller, H. G., and Gosman, A. D., "A Comparative Study of Subgrid Scale Models in Homogeneous Isotropic Turbulence," *Physics of Fluids*, Vol. 9, No. 5, 1997, pp. 1416–1429.
[34] Svennberg, U., and Fureby, C., "LES Computation of the Flow Over a Smoothly Contoured Ramp," AIAA Paper 2003-965, 2003.
[35] Persson, T., Liefevendahl, M., Bensow, R. E., and Fureby, C., "Numerical Investigation of the Flow over an Axisymmetric Hill Using LES, DES and RANS," *Journal of Turbulence*, Vol. 7, No. 4, 2006.
[36] Fureby, C., and Bensow, R. E., "LES at Work: Quality Management in Practical Large-Eddy Simulations," *ERCOFTAC Series*, Vol. 12, 2008, pp. 239–258.
[37] Wikström, N., Svennberg, U., Alin, N., and Fureby, C., "LES of the Flow Past an Inclined Prolate Spheroid," *Journal of Turbulence*, Vol. 5, No. 29, 2004.
[38] Karlsson, A., and Fureby, C., "LES of the Flow Past a Prolate Spheroid," AIAA Paper 2009-1616, 2009.
[39] Alin, N., Bensow, R. E., Fureby, C., Huuva, T., and Svennberg, U., "Current Capabilities of DES and LES for Submarines at Straight Course," *Journal of Ship Research*, Vol. 54, No. 3, 2010, pp. 184–196.
[40] Alin, N., Fureby, C., Parmhed, O., and Svennberg, U., "Large Eddy Simulation Past the DTMB 5415 Hull," *Proceedings of 27th Symposium on Naval Hydrodynamics*, Vol. 2, Seoul, Korea, 2008, pp. 217–231.
[41] Fureby, C., Grinstein, F. F., Li, G., and Gutmark, E. J., "An Experimental and Computational Study of a Multi-Swirl Gas Turbine Combustor," *Proceedings of the Combustion Institute*, Vol. 31, No. 2, 2007, pp. 3107–3114. doi:10.1016/j.proci.2006.07.127
[42] Fureby, C., "LES of a Multi-Burner Annular Gas Turbine Combustor," *Flow, Turbulence and Combustion*, Vol. 84, No. 3, 2010, pp. 543–564.
[43] Berglund, M., Fureby, C., Sabel'nikov, V., and Tegnér, J., "On the Influence of Finite Rate Chemistry in LES of Supersonic Combustion," *Proceedings of 32nd International Symposium on Combustion*, Montreal, Canada, 2008.
[44] Lourenco, L., and Shih, C., "Characteristics of the Plane Turbulent Near Wake of a Circular Cylinder. A Particle Image Velocimetry Study," 1993. (experimental data taken from [45]).
[45] Ma, X., Karamons, G.-S., and Karniadakis, G. E., "Dynamics and Low-Dimensionality of a Turbulent Near Wake," *Journal of Fluid Mechanics*, Vol. 410, 2000, pp. 29–65. doi:10.1017/S0022112099007934
[46] Ong, L., and Wallace, J., "The Velocity Field of the Turbulent Very Near Wake of a Circular Cylinder," *Experiments in Fluids*, Vol. 20, No. 6, 1996, pp. 441–453. doi:10.1007/BF00189383
[47] Tremblay, F., "Direct and Large-Eddy Simulation of Flow Around a Circular Cylinder at Subcritical Reynolds Number," Ph.D Dissertation, Fachgebiet Strömungsmechanik, Technische Univerität München, Munich, Germany, 2001.
[48] Cundy, H., and Rollett, A., "Lissajous's Figures," *Mathematical Models*, 3rd ed., Traquin, Stradbroke, England, U.K., 1997, pp. 242–244.

M. Visbal
Associate Editor